

Analytical solutions to the Grad–Shafranov equation for tokamak equilibrium with dissimilar source functions

P. J. Mc Carthy

Citation: [Phys. Plasmas](#) **6**, 3554 (1999); doi: 10.1063/1.873630

View online: <http://dx.doi.org/10.1063/1.873630>

View Table of Contents: <http://pop.aip.org/resource/1/PHPAEN/v6/i9>

Published by the [American Institute of Physics](#).

Related Articles

Enhancements to the JET poloidally scanning vacuum ultraviolet/visible spectrometers

[Rev. Sci. Instrum.](#) **83**, 10D536 (2012)

Anisotropic electron temperature measurements without knowing the spectral transmissivity for a JT-60SA Thomson scattering diagnostic

[Rev. Sci. Instrum.](#) **83**, 10E346 (2012)

Collisionless inter-species energy transfer and turbulent heating in drift wave turbulence

[Phys. Plasmas](#) **19**, 082309 (2012)

Paraxial Wentzel–Kramers–Brillouin method applied to the lower hybrid wave propagation

[Phys. Plasmas](#) **19**, 082510 (2012)

Identification of errors in the electron density measurements of a tangential interferometer/polarimeter system during a tokamak discharge

[Rev. Sci. Instrum.](#) **83**, 10E345 (2012)

Additional information on Phys. Plasmas

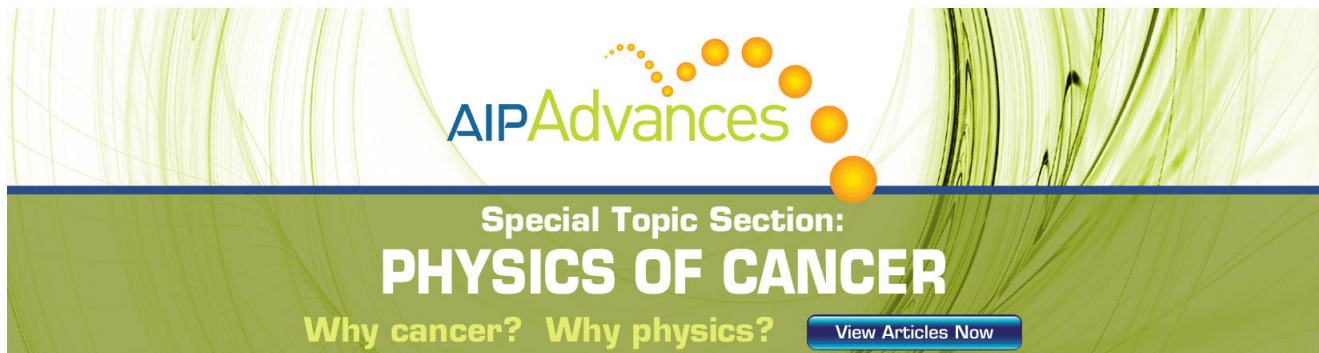
Journal Homepage: <http://pop.aip.org/>

Journal Information: http://pop.aip.org/about/about_the_journal

Top downloads: http://pop.aip.org/features/most_downloaded

Information for Authors: <http://pop.aip.org/authors>

ADVERTISEMENT



AIPAdvances

Special Topic Section:
PHYSICS OF CANCER

Why cancer? Why physics? [View Articles Now](#)

Analytical solutions to the Grad–Shafranov equation for tokamak equilibrium with dissimilar source functions

P. J. Mc Carthy^{a)}

Department of Physics, University College Cork, Association EURATOM-DCU, Cork, Ireland

(Received 29 April 1999; accepted 11 June 1999)

Exact solutions to the Grad–Shafranov equation for ideal magnetohydrodynamic (MHD) tokamak equilibria with dissimilar functional dependences of the pressure and poloidal current source profiles are presented. The current density profile has three free parameters, which is sufficiently flexible to describe equilibria consistent with external magnetic measurements. Experimental x -point and limiter plasma configurations can be represented by a superposition of solutions with the same eigenvalue. Both normal and reversed shear current profiles are allowed. An efficient algorithm for least squares fitting of numerically obtained experimental equilibria to the exact solution functions is described and applied to the ASDEX Upgrade (axially symmetric divertor experiment) tokamak [Plasma Physics and Controlled Nuclear Fusion Research 1992 (International Atomic Energy Agency, Vienna, 1993), Vol. I, p. 127]. © 1999 American Institute of Physics. [S1070-664X(99)03209-7]

I. INTRODUCTION

The simplest useful mathematical model of fusion plasmas is given by the set of magnetohydrodynamic (MHD) equations^{1,2} which provide a fluid description of macroscopic plasma behavior. For stationary and ideally conducting plasmas this description simplifies to a single vector equation of force balance together with Maxwell's equations

$$\mathbf{J} \times \mathbf{B} = \nabla p, \quad \nabla \times \mathbf{B} = \mu_0 \mathbf{J}, \quad \nabla \cdot \mathbf{B} = 0, \quad (1)$$

where \mathbf{J} and \mathbf{B} are the current density and magnetic induction fields, μ_0 is the vacuum permeability and p is the fluid pressure in the plasma. For axially symmetric configurations, where $\partial/\partial\phi=0$ in the cylindrical coordinate system R, ϕ, Z , Eq. (1) reduces to the scalar partial differential equation commonly referred to as the Grad–Shafranov equation^{3,4} (GSE)

$$-\left(\frac{\partial^2 \psi}{\partial R^2} - \frac{1}{R} \frac{\partial \psi}{\partial R} + \frac{\partial^2 \psi}{\partial Z^2}\right) = \mu_0 R^2 p'(\psi) + FF'(\psi) \\ \equiv \mu_0 R j_\phi, \quad (2)$$

where j_ϕ is the toroidal current density. Here the stream function ψ is the poloidal magnetic flux per radian, $F = RB_\phi = \mu_0 I_{\text{pol}}(\psi)/2\pi$ where I_{pol} is the poloidal current, and $p'(\psi) = dp/d\psi$ and $FF'(\psi) = d(\frac{1}{2}F^2)/d\psi$ are arbitrary functions of ψ . The left-hand side of Eq. (2) is usually written with a Laplacian-type symbol: $-\Delta^*\psi$. Exact solutions to the GSE are an aid to theoretical investigations into plasma equilibrium, stability, and transport in axisymmetric plasmas. For example, their use in stability analysis can remove the need for expansions about straight cylinder solutions in the inverse aspect ratio $\epsilon = a/R_p$ (a and R_p are the minor and major radii of the plasma, respectively) and tasks such as following particle trajectories are not subject to finite grid

resolution and other problems associated with numerical solutions. On the other hand, existing exact solutions are very restricted in the variety of allowed current density profiles. In particular, the pressure and squared poloidal current source profiles have the same functional dependence on the solution function ψ , namely either both are linear in ψ or both are quadratic in ψ . Here, we present a new family of solutions where $p(\psi) \propto \psi$ and $FF(\psi) \propto \psi^2 + \gamma\psi$. This has the advantage that both peaked and hollow current profiles are allowed, and it becomes feasible to fit realistic experimental configurations with exact solution functions.

We adopt a practical approach to applying the new solutions to experimental equilibrium configurations: Starting with a conventional numerical solution of the GSE, a least squares best fit to the flux function on and inside the plasma boundary is performed using a linear superposition of terms satisfying the GSE with a given eigenvalue which is iteratively optimized.

The paper is organized as follows. In Sec. II we review existing exact solutions to the GSE and introduce the new family. In Sec. III, the algorithm for fitting an exact solution to an experimental equilibrium obtained by numerical solution of the GSE is outlined and its application is illustrated with examples from the ASDEX Upgrade tokamak (Axially Symmetric Divertor Experiment).⁵ Some discussion and conclusions are presented in the final section.

II. ANALYTICAL SOLUTIONS TO THE GSE

A. The Solov'ev equilibrium

The simplest analytical solution to the inhomogeneous GSE, the Solov'ev equilibrium,⁶ corresponds to source functions linear in ψ :

$$p(\psi) = (A/\mu_0)\psi, \quad F^2(\psi) = 2B\psi + F_0^2, \quad (3)$$

^{a)}Electronic mail: pjm@ucc.ie

where $F_0 = \mu_0 I_0 / 2\pi$ is the vacuum contribution to $F(\psi)$ and A and B are also constants. The GSE reduces to

$$-\Delta^* \psi = AR^2 + B, \quad (4)$$

so that the toroidal current density profile takes the form

$$\mu_0 j_\phi = AR + B/R. \quad (5)$$

Equation (4) has the solution

$$\psi = \psi_{\text{vac}} - AR^4/8 - BZ^2/2, \quad (6)$$

where ψ_{vac} is any solution of the homogeneous equation $-\Delta^* \psi = 0$. The Solov'ev equilibrium has been widely used in studies of plasma equilibrium, transport and MHD stability analysis. By an appropriate choice of ψ_{vac} in Eq. (6), a wide variety of plasma shapes can be generated.⁷ The current profile itself is severely restricted, however, since the two free parameters A and B allow one to choose only the plasma (toroidal) current I_p and β_{pol} , the ratio of the volume-averaged particle pressure to the average poloidal magnetic field pressure along the plasma boundary. The shape of the current profile is essentially flat, with $\mu_0 j_\phi$ tending to the constant value $AR_p + B/R_p$ for $R_p/a \gg 1$.

B. The Herrnegger-Maschke solutions

Herrnegger⁸ and Maschke⁹ first found solutions to the GSE for parabolic source functions

$$p(\psi) = (C/\mu_0)\psi^2/2, \quad F^2(\psi) = D\psi^2 + F_0^2. \quad (7)$$

In this case the GSE becomes

$$-\Delta^* \psi = CR^2\psi + D\psi, \quad (8)$$

where the toroidal current density profile is given by $\mu_0 j_\phi = (CR + D/R)\psi$. By making the substitution $R^2 = 2X/\sqrt{C}$, Eq. (8) can be re-expressed as

$$2\sqrt{C}X \frac{\partial^2 \psi}{\partial X^2} + \frac{\partial^2 \psi}{\partial Z^2} + (2\sqrt{C}X + D)\psi = 0. \quad (9)$$

This is a linear homogeneous equation which, under appropriate boundary conditions, is separable in X and Z , say $\psi = G(X)H(Z)$. The equation in Z then becomes $H''(Z)/H(Z) = -k^2$, say, so that for the X dependence we obtain, on dividing across by $2\sqrt{C}$,

$$\frac{\partial^2 G}{\partial X^2} + \left(1 - \frac{2\eta}{X}\right)G = 0, \quad (10)$$

where $\eta = (k^2 - D)/4\sqrt{C}$. This is the differential equation for the Coulomb wave functions $F_0(\eta, X)$ and $G_0(\eta, X)$.¹⁰ Thus we have

$$\psi(R, Z) = \alpha(F_0(\eta, X) + \gamma G_0(\eta, X))\cos(kZ), \quad (11)$$

where the Z dependence is chosen to be symmetric about $Z = 0$.

Using pseudo-analytic function theory, De Menna¹¹ has generated recursive sequences of exact solutions starting with the Herrnegger-Maschke (HM) solutions. Only in the case of the simplest HM solution, however, namely for $\eta = 0$ in Eq. (10) which yields $\psi = \psi_0 \cos(X - X_0)\cos(kZ)$, does this procedure yield some simple analytical expressions.

Like the Solov'ev equilibrium, the HM parameterization of j_ϕ has only two free parameters [C and D in Eq. (8)] which allow independent specification of, e.g., β_{pol} and I_p ; and while the current profile here has a parabolic spatial dependence, this shape is again essentially fixed.

C. An analytical solution with dissimilar source functions

Here we introduce a new analytical solution to the GSE by specifying dissimilar functional dependences of the source profiles on the stream function, namely

$$p(\psi) = (S/\mu_0)\psi, \quad F^2(\psi) = T\psi^2 + 2U\psi + F_0^2, \quad (12)$$

where S , T , U (and F_0^2) are constants. In this case the GSE becomes

$$-\Delta^* \psi = SR^2 + T\psi + U, \quad (13)$$

where the toroidal current density profile is given by

$$\mu_0 j_\phi = SR + T\psi/R + U/R. \quad (14)$$

To solve Eq. (13) we first note that the terms $SR^2 + U$ satisfy $-\Delta^*(SR^2 + U) = 0$ and then proceed to solve the more tractable homogeneous equation and eigenvalue problem

$$-\Delta^* \psi_h = T\psi_h. \quad (15)$$

Once ψ_h is found, we construct solutions to Eq. (13) by setting $\psi = \psi_h - SR^2/T - U/T$, for then we obtain

$$-\Delta^* \psi = T\psi_h = T\psi + SR^2 + U.$$

We seek solutions for ψ_h assuming separability in R and Z , i.e., $\psi_h = G(R)H(Z)$, and obtain, on setting $H''(Z) = -k^2 H(Z)$

$$H''(Z) + k^2 H(Z) = 0, \quad (16)$$

$$G''(R) - \frac{G'(R)}{R} - (k^2 - T)G(R) = 0. \quad (17)$$

The solution for $H(Z)$ is given by $H(Z) = c_1 e^{ikZ} + c_2 e^{-ikZ}$ where c_1 and c_2 are arbitrary constants of integration. The differential equation for $G(R)$ is solved by noting the following relations involving Bessel functions:¹²

$$\pm B_{n+1}(aR) = \frac{2n}{aR} B_n(aR) - B_{n-1}(aR), \quad (18)$$

$$B'_n(aR) = \frac{a}{2} (B_{n-1}(aR) \mp B_{n+1}(aR)), \quad (19)$$

$$B_{-n}(aR) = (\mp)^n B_n(aR), \quad (20)$$

where B are the Bessel functions J and Y for the first choice of sign, and the modified Bessel functions I and K for the second choice. Consider now $g(R) = RB_1(aR)$ where a is a parameter. Straightforward application of Eqs. (18)–(20) leads to

$$g'(R) = aRB_0(aR), \quad (21)$$

$$g''(R) = aB_0(aR) \mp a^2 RB_1(aR), \quad (22)$$

$$g''(R) - g'(R)/R - (k^2 - T)g(R) = (T - k^2 \mp a^2)g(R), \quad (23)$$

and hence we have shown that

$$\psi_h(R, Z) = RB_1(aR)(c_1 e^{ikZ} + c_2 e^{-ikZ}) \quad (24)$$

satisfies Eq.(15) when a satisfies

$$a^2 = \pm(T - k^2), \quad (25)$$

where $+$ applies to the $J_1(aR)$, $Y_1(aR)$ and $-$ to the $I_1(aR)$, $K_1(aR)$ Bessel functions.

Hence we find that Eqs. (24) and (25) generate the following families of real solutions for positive or negative T and real k

$$\psi_{h,1}(R, Z) = RJ|Y_1(\sqrt{T - k^2}R)(c_1 \cos kZ + c_2 \sin kZ), \quad 0 \leq k^2 \leq T, \quad T > 0, \quad (26)$$

$$\psi_{h,2}(R, Z) = RJ|Y_1(\sqrt{T + k^2}R)(c_1 \cosh kZ + c_2 \sinh kZ), \quad \begin{cases} 0 \leq k^2 < \infty; & T > 0 \\ -T \leq k^2 < \infty; & T < 0, \end{cases} \quad (27)$$

$$\psi_{h,3}(R, Z) = RI|K_1(\sqrt{-T + k^2}R)(c_1 \cos kZ + c_2 \sin kZ), \quad \begin{cases} T \leq k^2 < \infty; & T > 0 \\ 0 \leq k^2 < \infty; & T < 0, \end{cases} \quad (28)$$

$$\psi_{h,4}(R, Z) = RI|K_1(\sqrt{-T - k^2}R)(c_1 \cosh kZ + c_2 \sinh kZ), \quad 0 \leq k^2 < -T; \quad T < 0, \quad (29)$$

where $J|Y$ denotes J or Y , etc. and the hyperbolic solutions correspond to imaginary k in Eq. (24). Additional solutions outside this scheme arise when either $G(R)$ or $H(Z)$ satisfy the homogeneous GSE. This yields

$$\psi_{h,5}(R, Z) = \begin{cases} RJ|Y_1(\sqrt{T}R)(c_1 + c_2 Z); & T > 0 \\ RI|K_1(\sqrt{-T}R)(c_1 + c_2 Z); & T < 0, \end{cases} \quad (30)$$

$$\psi_{h,6}(R, Z) = \begin{cases} c_1 \cos \sqrt{T}Z + c_2 \sin \sqrt{T}Z; & T > 0 \\ c_1 \cosh \sqrt{-T}Z + c_2 \sinh \sqrt{-T}Z; & T < 0, \end{cases} \quad (31)$$

$$\psi_{h,7}(R, Z) = \begin{cases} R^2(c_1 \cos \sqrt{T}Z + c_2 \sin \sqrt{T}Z); & T > 0 \\ R^2(c_1 \cosh \sqrt{-T}Z + c_2 \sinh \sqrt{-T}Z); & T < 0. \end{cases} \quad (32)$$

Finally, the following solution to Eq. (15), is based not on separability but rather on the relation $\Delta^* f(\rho) = f''(\rho)$ where $\rho = \sqrt{R^2 + Z^2}$

$$\psi_{h,8}(R, Z) = \begin{cases} c_1 \cos \sqrt{T(R^2 + Z^2)} + c_2 \sin \sqrt{T(R^2 + Z^2)}; & T > 0 \\ c_1 \cosh \sqrt{-T(R^2 + Z^2)} + c_2 \sinh \sqrt{-T(R^2 + Z^2)}; & T < 0. \end{cases} \quad (33)$$

Note that complex k values in Eqs. (26)–(29) leading to complex Bessel function arguments yield unwieldy complex solutions, since, e.g., $J_1(z) = J_1(x + iy)$ then becomes¹³

$$J_1(x + iy) = \sum_{p=-\infty}^{\infty} J_p(x) J_{1-p}(iy) = \sum_{p=-\infty}^{\infty} (i)^{1-p} J_p(x) I_{1-p}(y), \quad (34)$$

and we will not consider such solutions here.

In contrast to previous analytical solutions, the present family has a current profile with three independent parameters so that it is now possible to independently specify I_p , β_{pol} , and one shape moment of j_ϕ such as the internal inductance l_i . This offers the possibility of fitting experimental configurations in a manner consistent with external magnetic measurements, since it is generally observed that the latter are insensitive to higher moments of the current profile.¹⁴

III. EXACT REPRESENTATION OF FREE BOUNDARY SOLUTIONS TO THE GSE

We wish to use the exact solutions to Eq. (13) presented here to describe experimentally relevant equilibrium configurations. The straightforward method of doing this would be to first define boundary conditions and then determine the eigenvalues T for which the solution functions satisfy the boundary conditions. There is, however, a fundamental difficulty with this approach when we need to solve a free boundary problem with both plasma and vacuum regions. The exact solution is valid only on and inside the plasma boundary [the right hand side of Eq. (13) vanishes in the vacuum region], but the boundary is not *a priori* known, since it is determined by the solution. We overcome this difficulty by (i) numerically solving the free boundary problem (with a conventional equilibrium solver) for Eq. (13) and (ii) projecting the numerically calculated solution onto the exact solutions via a least squares fitting procedure.

Step (i) is carried out using the following formulation of the problem: The equilibrium is a solution of the GSE [for the particular form of j_ϕ given in Eq. (14)] with known additional sources (in the form of external poloidal field coil currents) for the flux function ψ and boundary conditions at infinity and at $R = 0$. The algorithm to solve the problem on an unbounded domain, which uses an efficient Greens function method to determine the boundary flux which cancels artificial boundary conditions¹⁵ imposed on the perimeter of the finite computational domain, was developed by Lackner¹⁶ and forms the central element of the Garching Equilibrium Code.¹⁶

The rationale for step (ii) is our anticipation that a linear superposition of functions satisfying Eq. (15) for a given eigenvalue T drawn from the relevant seven families of solutions tabulated in Eqs. (26)–(33) will suffice to accurately describe the shape of the numerically obtained flux surfaces in much the same way as vacuum solutions were combined with the basic Solov'ev solution to yield a desired plasma shape in Ref. 7.

Assuming the fit to the numerical solution is for practical purposes exact (the criterion is defined below), this strategy yields an analytic solution to the free boundary problem

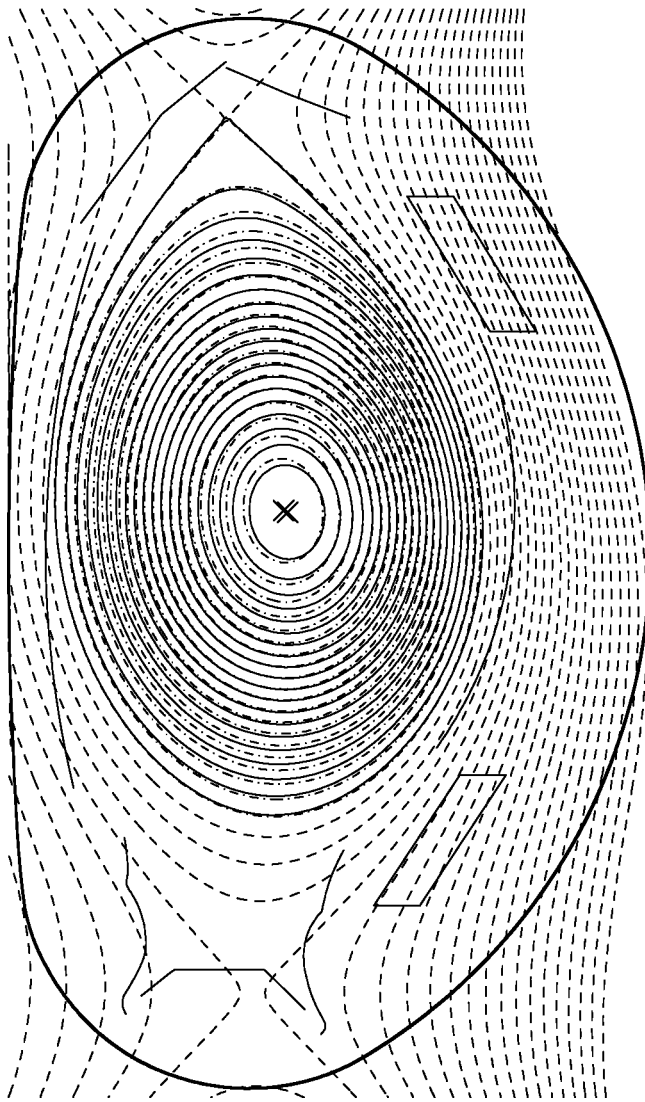


FIG. 1. CLISTE interpretive equilibrium (solid and dashed contours denote the plasma and vacuum flux surfaces, respectively) and exact GSE solution (dot-dashed contours in the plasma region, vacuum contours not drawn) for ASDEX Upgrade discharge # 10 966, $t = 1.242$ s.

which is valid in the plasma region. The motivation for seeking such solutions has already been outlined in the Introduction.

We now proceed to describe an efficient algorithm for a least squares best fit of an existing numerical solution of the GSE to the new class of exact solutions. The method is then applied to examples of experimental equilibrium configurations from the ASDEX Upgrade tokamak.

A. Least squares fitting algorithm

Each family of solutions in Eqs. (26)–(30) consists of four separate functions, e.g., for Eq. (26) we have $\{R J_1(\alpha R) \cos kZ, R J_1(\alpha R) \sin kZ, R Y_1(\alpha R) \cos kZ, R Y_1(\alpha R) \sin kZ\}$ where $\alpha = \sqrt{T - k^2}$. [Equations (31)–(33) consist of two functions each.] In the case of Eqs. (26)–(29) each individual solution moreover has two parameters α and k constrained by $\pm \alpha^2 \pm k^2 = T$, the choice of signs being determined by the solution family and the sign of T . For the

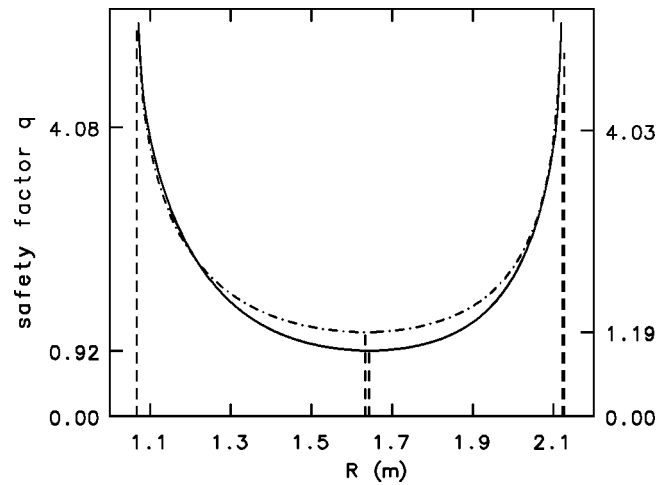


FIG. 2. $q(R, Z_{\text{mag.axis}})$, the q profile across the plasma diameter on a horizontal chord passing through the magnetic axis for the CLISTE (solid) and exact GSE (dot-dashed) equilibrium solutions shown in Fig. 1. The $q_{95\%}$ and q_0 values are marked on the left (CLISTE) and right (exact GSE solution) hand axes. Vertical dashed lines mark the plasma boundary and the magnetic axis. Figures 1 and 2 are on the same scale.

case of Eq. (26) where the constraint is given by $\alpha^2 + k^2 = T$, each of the four individual solutions may lie anywhere on a circle of radius $p = \sqrt{T}$ in the α, k parameter plane.

To utilize the freedom offered by a range of allowable parameter values, we choose a number of discrete values of k to construct a sequence of independent solutions from a given solution function (solutions involving integrals over k are also possible). If n_k functions are required, the geometric picture suggests choosing $\tan k/\alpha = i\pi/2(n_k + 1)$, ($i = 1, \dots, n_k$), i.e., equidistantly spaced in the first quadrant of the circle and excluding the endpoints $k = 0$, $k = p$ since these cases are already catered for in Eqs. (30)–(31). In the applications discussed below, the choice of n_k is a trade-off between accuracy and model size.

Given a prescribed discretization scheme for k such as that just discussed, Eqs. (26)–(33) are linear in all free parameters with the exception of the eigenvalue T . A least squares regression problem where some of the free parameters are *conditionally linear*¹⁷ can be efficiently tackled using the following scheme: (i) Iterate the nonlinear parameter(s), (ii) given the latest set of nonlinear parameter(s), choose optimum values of the linear parameters by performing a *linear* least squares regression.

Using this scheme, a suitably large set of exact solution functions drawn from Eqs. (26)–(33) can be projected onto a numerical solution to the GSE in the form of a grid of poloidal flux values. Since Eq. (13) applies on and inside the plasma boundary only, we exclude the vacuum region of the grid from the fit. For the examples discussed below, we solved the GSE numerically on a 129×257 grid of which the order of 5000 gridpoints lying inside the plasma boundary were included in the fit. The function to be minimized is just the sum of squared differences over these gridpoints between ψ as given by the numerical solution and ψ as given by the linear combination of the selected set of solution functions whose coefficients [the c_1 and c_2 's in Eqs. (26)–(33) to-

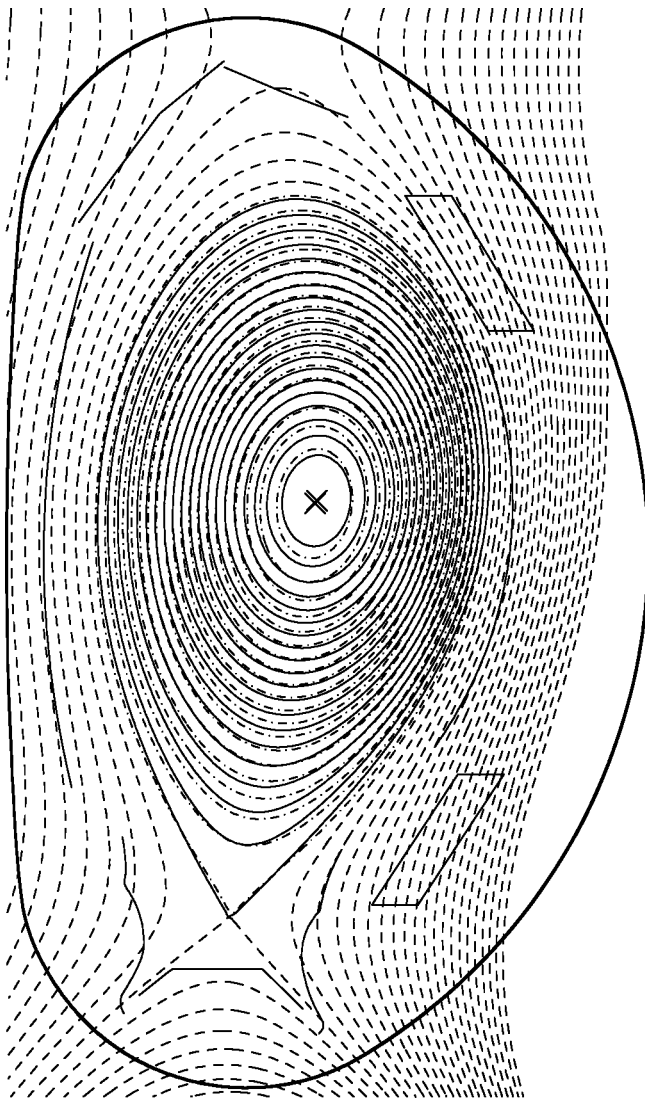


FIG. 3. CLISTE interpretive equilibrium and exact GSE solution for ASDEX Upgrade discharge # 10 958, $t = 5.200$ s.

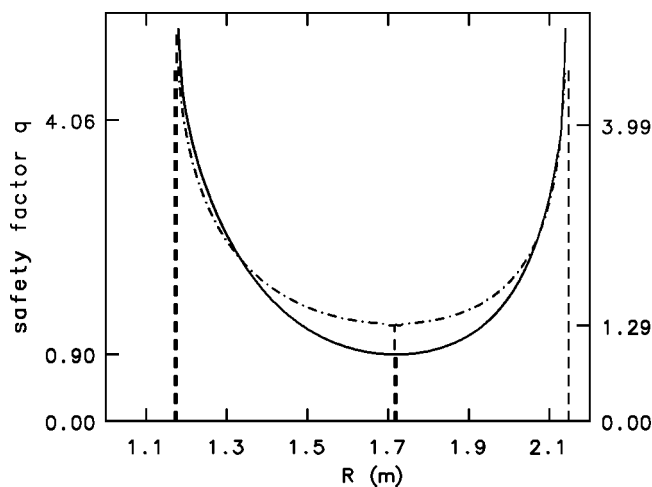


FIG. 4. $q(R, Z_{\text{mag,axis}})$ for the CLISTE and exact GSE equilibrium solutions shown in Fig. 3.

gether with the eigenvalue T] are the free parameters of the fit. For a sufficiently close fit, e.g., one where the error is comparable to the convergence error in the numerical solution, the exact representation inside the boundary will be consistent with the vacuum solution outside.

B. Application to the ASDEX Upgrade tokamak

In this subsection, we present both interpretive and predictive equilibria, the differences between which we now outline in the interests of clarity. An interpretive equilibrium is characterized by a j_ϕ profile with *free* parameters whose values are optimized so as to yield a best fit to a set of experimental measurements—typically magnetic probe and flux loop signals. A predictive equilibrium, in contrast, has a j_ϕ profile with *fixed* parameters; hence the problem is already fully specified and the question of consistency with experimental measurements does not apply (the treatment of the external coil currents is identical in both cases, unless due to uncertainties in the current measurement the currents themselves are also allowed to float in the interpretive ap-

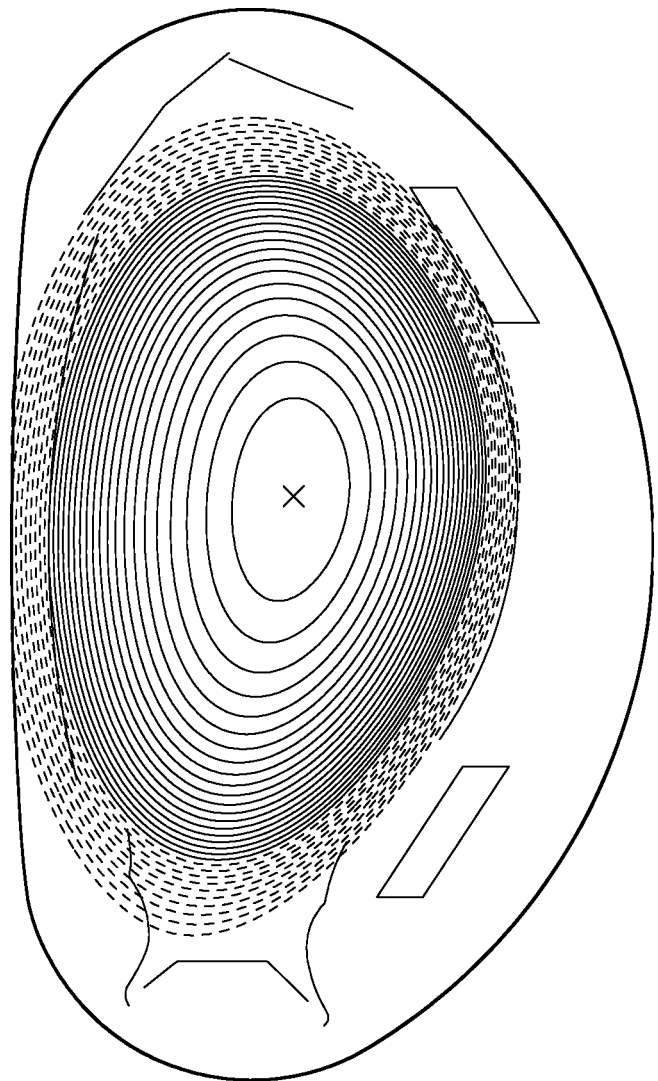


FIG. 5. Exact GSE solution (solid contours) and vacuum flux contours (dashed) for a predictive reversed shear ASDEX Upgrade equilibrium.

proach). In both cases, the algorithm to solve for an equilibrium is similar, the difference being that whereas in the case of a predictive equilibrium calculation the flux surface topology (in particular the plasma boundary) is iterated for a fixed j_ϕ profile parameterization, both the flux function and the parameters of the j_ϕ profile are iterated during an interpretive calculation.

The solid curves in Fig. 1 are poloidal flux contours of an interpreted equilibrium calculated by the CLISTE interpretive equilibrium code¹⁸ using a spline parameterization of j_ϕ with three free parameters during an Ohmically heated phase of ASDEX upgrade upper x -point discharge # 10966, $t=1.242$ s, $I_p=0.8$ MA, $B_\phi=-2.0$ T, $\beta_{pol}=0.24$. The solid curve in Fig. 2 is the corresponding q profile. The rms (root mean square) magnetic field error for the 49 in-vessel equilibrium magnetic signals used in the fit is 1.3 mT corresponding to 0.9% of the rms signal magnitude. Allowing additional free spline parameters made no significant improvement to the fit for this equilibrium. The dot-dashed contours in Fig. 1 belong to an interpretation of the same data, this time with j_ϕ prescribed by Eq. (14). The dot-dashed curve in Fig. 2 is the corresponding q profile. Here the rms field error was 1.7 mT or 1.2% of the rms signal magnitude. The typical spatial separation between corresponding flux surfaces is ≤ 5 mm for the separatrix contour, 15 mm in the neighborhood of the magnetic axis and rises to

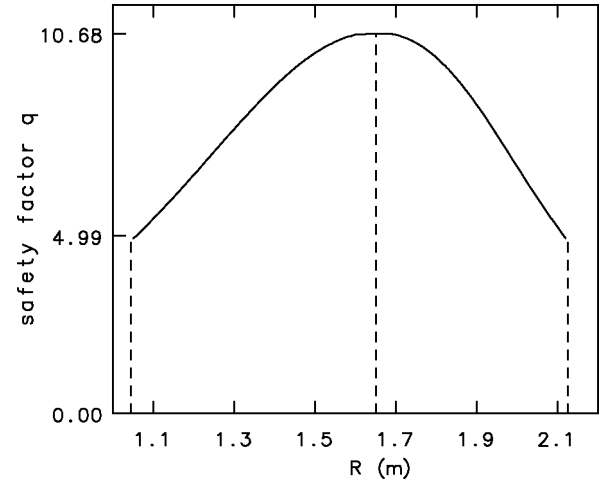


FIG. 6. $q(R, Z_{mag, axis})$ for the predictive equilibrium solution shown in Fig. 5.

3 cm for most of the flux surfaces between axis and separatrix.

Using the algorithm outlined in Sec. III A above, the dot-dashed poloidal flux function shown in Fig. 1 was fitted to the convergence accuracy of the equilibrium calculation (rms error ≈ 1 mVs) with the following exact solution to the GSE:

$$\begin{aligned} \psi(R, Z) = & c_1 + c_2 R^2 + R J_1(pR)(c_3 + c_4 Z) + c_5 \cos pZ + c_6 \sin pZ + R^2(c_7 \cos pZ + c_8 \sin pZ) + c_9 \cos p\sqrt{R^2 + Z^2} \\ & + c_{10} \sin p\sqrt{R^2 + Z^2} + R J_1(vR)(c_{11} \cos qZ + c_{12} \sin qZ) + R J_1(qR)(c_{13} \cos vZ + c_{14} \sin vZ) \\ & + R Y_1(vR)(c_{15} \cos qZ + c_{16} \sin qZ) + R Y_1(qR)(c_{17} \cos vZ + c_{18} \sin vZ), \end{aligned} \quad (35)$$

where $T=17.8116$ is the eigenvalue, $p=\sqrt{T}=4.22038$, $q=p/2$, $v=p\sqrt{3}/4$ (corresponding to $n_k=2$ yielding $\tan k/\alpha=30^\circ, 60^\circ$ —see paragraph two of this subsection) and the vector of coefficients c_1-c_{18} is given by

$$\begin{aligned} \mathbf{c} = & [0.17795, -0.03291, 1.4934, -0.4818, -1.1759, \\ & -0.1620, 0.3722, 0.07697, 1.2959, 0.5881, 1.5820, \\ & -0.009059, 2.2388, 0.4186, 1.1950, \\ & -0.4265, 0.8057, -0.004804]. \end{aligned}$$

This expression yields ψ in Vs, so the current density in units of MA m^{-2} is given by

$$j_\phi = \frac{T(\psi - c_1 - c_2 R^2)}{\mu_0(2\pi R) \times 10^6} = \frac{T(\psi - c_1 - c_2 R^2)}{0.8\pi^2 R}. \quad (36)$$

It is important to note that the differences between the solid and dot-dashed contours in Fig. 1 result from the different j_ϕ parameterizations used to solve the interpretive equilibrium problem. Both solutions are of good quality as evidenced by the low ($\approx 1\%$) disagreement between fitted and experimental magnetic measurements. The fit represented by the solid contours is, however, noticeably superior (the rms

error is 25% lower) and is presented here as a benchmark against which the fit using the ansatz given in Eq. (14) may be judged. We emphasize that the fit to the numerical solution represented by the dot-dashed contours using the analytical expression Eq. (35) is, for practical purposes, *exact*.

The solid contours in Fig. 3 are those of an interpreted equilibrium from the neutral beam heated ASDEX Upgrade lower x -point discharge # 10958 $t=5.200$ s, $I_p=1.0$ MA, $B_\phi=-2.5$ T, $\beta_{pol}=1.07$. The solid curve in Fig. 4 is the corresponding q profile. A good fit to the magnetic data is obtained here with CLISTE using a polynomial model with four free parameters: $R j_\phi = aR^2 + b + c\psi + d\psi^2$ and the rms magnetic field error for the 49 equilibrium magnetic signals used in the fit is 1.3 mT corresponding to 0.6% of the rms signal magnitude. The dot-dashed contours in Fig. 3 is an interpretation of the same data, with j_ϕ prescribed by Eq. (14), equivalent to forcing $d=0$ in the CLISTE polynomial model. The dot-dashed curve in Fig. 4 is the corresponding q profile. Here the rms field error is 1.9 mT or 0.9% of the rms signal magnitude. The spatial separation between corresponding flux surfaces is ≤ 15 mm for both separatrix and magnetic axis regions and again rises to 3 cm for most of the flux surfaces between axis and separatrix. The vector of co-

efficients of the exact solution Eq. (35) fitted to the dot-dashed contour ψ function shown in Fig. 3 is given by

$$\mathbf{c}=[0.4733,-0.2164,0.0,0.0,0.0,0.0,-0.068\ 30,0.012\ 20,0.1687,0.8635,-1.0682,0.021\ 66,-0.002\ 662,0.1178,1.4008, \\ -0.2656,1.3770,0.2468],$$

where in this case $T=15.2329$ is the eigenvalue.

An example of a predictive reversed shear equilibrium using ASDEX upgrade field coils and vessel geometry is shown in Fig. 5 and the corresponding q profile is shown in Fig. 6. Here $I_p=1$ MA, $B_\phi=2.5$ T, $\beta_{\text{pol}}=0.33$, $l_i=0.30$ $q_0=10.6$, $q_{\text{min}}=4.9$, and the exact solution inside the plasma boundary is given by

$$\psi(R,Z)=c_1+c_2R^2+R I_1(pR)(c_3+c_4Z)+c_5 \cosh pZ+c_6 \sinh pZ+R^2(c_7 \cosh pZ+c_8 \sinh pZ) \\ +c_9 \cosh p \sqrt{R^2+Z^2}+c_{10} \sinh p \sqrt{R^2+Z^2}+R I_1(vR)(c_{11} \cosh qZ+c_{12} \sinh qZ)+R I_1(qR)(c_{13} \cosh vZ \\ +c_{14} \sinh vZ)+R K_1(vR)(c_{15} \cosh qZ+c_{16} \sinh qZ)+R K_1(qR)(c_{17} \cosh vZ+c_{18} \sinh vZ), \quad (37)$$

where $T=-21.955$ is the eigenvalue, $p=\sqrt{-T}=4.6856$, $q=p/2$, $v=p \sqrt{3/4}$ and the vector of coefficients c_1-c_{18} is given by

$$\mathbf{c}=[0.5162,0.072\ 44,-0.001\ 694,-0.000\ 2904,0.009\ 665,-0.058\ 58,-0.014\ 07,0.030\ 05,-26.794\ 69,26.796\ 09, \\ -0.004\ 090,0.000\ 8088,-0.001\ 209,-0.005049,-39.0417,-6.2964,0.035\ 97,0.8877].$$

IV. CONCLUSIONS

We have presented a new family of exact solutions to the Grad-Shafranov equation which for the first time, to our knowledge, has a current density parameterization with three degrees of freedom, allowing an independent choice of I_p , β_{pol} , and l_i . The Solov'ev j_ϕ parameterization is a special case of the present one, as can be seen by comparing Eqs. (5) and (14). In Sec. III A we described an efficient algorithm to perform a hybrid linear-nonlinear least squares fit (with just one nonlinear parameter, namely the eigenvalue T) to a numerical solution to the free boundary equilibrium problem for the GSE. In Sec. III B we applied this algorithm (execution time: About 1 s on a sparc ultra workstation) to two experimental and one predictive ASDEX Upgrade equilibria which featured lower x -point, upper x -point and limiter configurations, low and high β_{pol} values, and normal and reversed shear current profiles. In all cases, the poloidal flux function in the plasma region was fitted, to the same numerical precision as the equilibrium solver, with an exact solution to the GSE involving less than 20 coefficients. In the case of the two experimental equilibria, the separatrix and near-axis flux surface geometry agreed to within 15 mm, or 3% of the minor radius, with accurate equilibrium interpretations using more flexible parameterizations of the current density profile. This agreement deteriorated by a factor of 2 for the region between axis and separatrix, however.

Thus, within the accuracies just cited, the family of exact solutions to the GSE presented here allows a realistic and compact description of experimental flux surface geometry as well as qualitatively describing the shape of the current density profile.

ACKNOWLEDGMENTS

The author is grateful to F. Herrnegger (IPP) and F. Holland and J. Grannell (UCC) for useful discussions. Section

III has benefitted from helpful suggestions made by the anonymous referee. This work was supported by a research agreement between the Max Planck Institut für Plasma-physik, Garching and University College Cork, and by EURATOM.

¹V. D. Shafranov, in *Reviews of Plasma Physics*, edited by M. A. Leontovich (Consultants Bureau, New York, 1975), Vol. 2.

²J. P. Freidberg, *Rev. Mod. Phys.* **54**, 801 (1982).

³V. D. Shafranov, *Sov. Phys. JETP* **6**, 545 (1958); *Zh. Eksp. Teor. Fiz.* **33**, 710 (1957).

⁴H. Grad and H. Rubin, in *Proceedings of the Second United Nations Conference on the Peaceful uses of Atomic Energy* (United Nations, Geneva, 1958), Vol. 21, p. 190.

⁵W. Köppendörfer, C. Andelfinger, M. Ballico, and the ASDEX Upgrade and NBI Teams, *Proceedings of the 14th Conference on Plasma Physics and Controlled Nuclear Fusion Research, 1992, Würzburg* (International Atomic Energy Agency, Vienna, 1993), Paper IAEA-CN-56/A-2-3, Vol. I, p. 127.

⁶L. S. Solov'ev, *Sov. Phys. JETP* **26**, 400 (1968); *Zh. Eksp. Teor. Fiz.* **53**, 626 (1967).

⁷S. B. Zheng, A. J. Wooton, and E. R. Solano, *Phys. Plasmas* **3**, 1176 (1996).

⁸F. Herrnegger, *Proceedings of 5th European Conference on Controlled Fusion and Plasma Physics*, Grenoble (European Physical Society, Petit Lancy, 1972), Vol. I, p. 26.

⁹E. K. Maschke, *Plasma Phys.* **15**, 535 (1972).

¹⁰M. Abramowitz and I. A. Stegun, *Handbook of Mathematical Functions* (Dover, New York, 1965), p. 538.

¹¹L. De Menna, *Nucl. Fusion* **17**, 455 (1977).

¹²M. Abramowitz and I. A. Stegun, *Handbook of Mathematical Functions* (Dover, New York, 1965), p. 361.

¹³Z. X. Wang and D. R. Guo, *Special Functions* (World Scientific, Singapore, 1989), p. 362.

¹⁴L. L. Lao, H. St. John, R. D. Stambaugh, A. G. Kellman, and W. Pfeiffer, *Nucl. Fusion* **25**, 1611 (1985).

¹⁵S. V. Tsynkov, *Appl. Numer. Math.* **27**, 465 (1998).

¹⁶K. Lackner, *Comput. Phys. Commun.* **12**, 33 (1974).

¹⁷D. M. Bates, *Nonlinear Regression Analysis and its Applications* (Wiley, New York, 1988), p. 85.

¹⁸P. J. Mc Carthy, P. Martin, W. Schneider, *Rep. 5/85* (1999) Max-Planck-Institut für Plasmaphysik, Garching.